

Nanobelts-constructed Porous TiO₂-B@SnS₂ Heterostructure Hybrids for Enhance Lithium Storage Performance

Chao Cai

Ningxia university

Meiyu Song

Ningxia university

Qixiang Ou

University of Minnesota

Jianmei Li

Ningxia university

changsheng an (✉ z20190628@ccsu.edu.cn)

Changsha University

Research Article

Keywords: Lithium-ion batteries, porous TiO₂-B nanobelts, heterostructure, electrochemical performance

Posted Date: March 25th, 2021

DOI: <https://doi.org/10.21203/rs.3.rs-356804/v1>

License:   This work is licensed under a Creative Commons Attribution 4.0 International License.

[Read Full License](#)

Abstract

Alloy-type anodes materials possess broad prospects for excellent electrochemical property lithium-ion batteries owing to its high theoretical capacity and excellent electronic conductivity. However, this type electrode materials experience poor kinetics and tremendous volume collapse during the repeated lithiation-delithiation process. Herein, an efficient method to provide a fast transmission channel and suppress the volume collapse during the discharge/charge process by constructing the heterostructure between porous TiO₂-B nanoblets and few-layer SnS₂ nanosheets interface, which provides high-active sites for the nucleation and growth of SnS₂ nanosheets, and inhibits the agglomeration of SnS₂ nanosheets. Both experimental results and theoretical calculations definite that porous TiO₂ nanobelts provides more chemical active sites for the adsorption and transmission of lithium ion and then effectively improve the stability the electrode structure. As a result, TiO₂-B@SnS₂ hybrid exhibits excellent rate and cycle performance. This work paves a way to design and construction of high performance alloy-type anode materials.

1. Introduction

Lithium ion batteries (LIBs) have been extensively used for portable electronics and electric vehicles, in terms of high energy density and long cycling performance^[1]. Currently, commercial graphite anode can hardly satisfy the increasing demand for LIBs' electrochemical performance due to its low discharge capacity and poor rate capability^[2]. Various electrode materials have been intensively investigated to achieve a high electrochemical performance, such as metallic oxide (TiO₂^[3], Co₃O₄^[4]), transition metal compounds (SnS₂^[5], MoS₂^[6]) and simple substance (P^[7], Si^[8]), et al. Among them, transition metal sulphide have attracted much attention due to their high theoretical capacity and excellent electronic conductivity ability^[1, 2]. In particular, as a typical 2D transition metal chalcogenides with a large interlayer spacing of 0.60 nm and weaker van der Waals interaction, SnS₂ demonstrates higher reversible capacities due to better kinetics^[1, 2, 9]. Unfortunately, similar to other alloy-type electrode materials, pure SnS₂ anode still suffers from inadequate rate property and large volumetric effect during the discharge/charge process due to the low intrinsic electronic conductivity and alloy reaction process^[1, 10-12].

So far, simple single-phase electrode materials are not enough to satisfy the requirement for reversible capacity and cycling stability^[11]. Many researchers have done a lot of research on the composite and structural design of electrode materials, such as carbon coating^[13-15], heterostructure construction^[1] and defective construction^[16], et al. Conclusion, heterostructure construction has been proved to be an effective technical tool to improve the charge and electronic transfer kinetics and suppress the volume change during the electrochemical reaction process^[17, 18]. Mai et al.^[19] designed WS₂/ZnS heterojunctions that shows enhance ions and electronic diffusion kinetics. In additionally, Guo et al.^[20] constructed SnS/SnO₂ heterostructures with internal electric fields exchange between the SnS/SnO₂

interface, which can enhance the reversible degree of alloy reaction and boost the ions/electrons transport in the electrode material structure. Furthermore, Wu et al.^[1] designed H-TiO₂@SnS₂@PPy hybrids with PPy-coating SnS₂ nanosheets anchored on hydrogen treated TiO₂. The specific heterojunction structure not only can improve the Li⁺ diffusion kinetics, but also suppress the volume change during the lithiation/delithiation process. Additionally, among the different crystalline phases of TiO₂ materials, TiO₂-B has attracted much attention owing to the open channels in the lattice, which making Li⁺ easier to transport inside the crystal structure and faster discharge/charge capability than anatase or rutile^[21, 22]. Meanwhile, TiO₂-B possesses a higher theoretical capacity (335 mAh g⁻¹) than the other polymorphs of TiO₂^[21]. Che et al.^[21] synthesize TiO₂-B thin nanosheets with hierarchical porous structure. As an anode for LIBs, TiO₂-B electrode exhibits high reversible capacity, excellent cycling performance and superior rate capability.

In this study, the TiO₂-B@SnS₂ hybrids has been prepared by a simple hydrothermal method, as illustration in Scheme 1. First, nanobelts-constructed porous TiO₂-B nanobelts was prepared by two-step hydrothermal with NaOH and H₂SO₄ solution, respectively. Then, the SnS₂ and TiO₂-B@SnS₂ hybrids were synthesized by a one-step hydrothermal method, respectively. It is noted that thin SnS₂ nanosheets were uniformly coated on the surface of porous TiO₂-B nanobelts which offers many active sites for the nucleation and growth of SnS₂ nanosheets. Meanwhile, combined electrochemical performance and theoretical calculations, it is also well recognized that the heterojunction structure between the SnS₂/TiO₂-B interface is one of the most strategy of choice to improve the Li⁺ diffusion kinetics and suppress the volume change during the discharge/charge process. As an anode materials for LIBs, the as-prepared TiO₂-B@SnS₂ electrode materials exhibits improved electrochemical performance in terms of high rate capability and excellent cycling stability. More important, to fully explore the TiO₂-B@SnS₂ anode, it is necessary to understand the action mechanism of heterojunction structure so that improving its electrochemical performances.

2. Results And Discussion

XRD patterns of TiO₂-B nanobelts, SnS₂ nanosheets and TiO₂-B@SnS₂ hybrids are displayed in Fig. 1a. The diffraction peak position fully in agreement with the TiO₂-B phase (PDF#74-1940), 2T-type layered structure of SnS₂ (PDF#22-0951), respectively^[23]. Furthermore, no additional peaks were found in our samples, indicating the high purity of product. For TiO₂-B nanobelts, small amount of anatase phase was obtained during the treatment process. Furthermore, the Raman spectrum of TiO₂-B nanobelts, SnS₂ and TiO₂-B@SnS₂ is shown in Fig. 1b. The peaks at 142.8, 196.3, 395.8, 517.1, and 637.4 cm⁻¹ were good in agreement with the Raman characteristics of TiO₂-B nanobelts, and 310.7 cm⁻¹ correspond to the Raman characteristics of SnS₂^[24].

The morphology of $\text{TiO}_2\text{-B}$ nanobelts, SnS_2 and $\text{TiO}_2\text{-B@SnS}_2$ are confirmed by scanning electron microscopy (SEM). The $\text{TiO}_2\text{-B}$ nanobelts were 50–400 nm wide, about 18 nm thick and several micrometers in length. After the acid treatment, many potholes were formed on the surface of $\text{TiO}_2\text{-B}$ nanobelts (Fig. 2a). The potholes on the surface of $\text{TiO}_2\text{-B}$ nanobelts by acid-corroded process, which offers many active sites for the nucleation and growth of SnS_2 nanosheets. Typically, SEM images of $\text{TiO}_2\text{-B@SnS}_2$ heterostructures is shown in Figs. 2b and c. The thin SnS_2 nanosheets were uniformly coated on the surface of $\text{TiO}_2\text{-B}$ nanobelts. Compared to the micron flower-like structure assembled with thin SnS_2 nanosheets (Fig. 2d), the thin SnS_2 nanosheets were vertically distributed on $\text{TiO}_2\text{-B}$ nanobelts for $\text{TiO}_2\text{-B@SnS}_2$ heterostructure (Figs. 2b, c), leading to shorten Li^+ diffusion distance. This phenomenon indicated that $\text{TiO}_2\text{-B@SnS}_2$ heterostructure possesses excellent electrochemical performance.

The microstructure of the $\text{TiO}_2\text{-B@SnS}_2$ heterostructure was confirmed by transmission electron microscopy (TEM). The thin SnS_2 nanosheets covered the surface of porous TiO_2 nanobelts (Fig. 2a) because of the surface deficiency caused by the acid-corroded process (Figs. S1a, b). This phenomenon indicated that the excellent electronic conductivity of the $\text{TiO}_2\text{-B@SnS}_2$ heterostructure was effectively improved by the shorten Li^+ diffusion distance and high ionic conductivity of TiO_2 . A lattice fringe with a d-spacing of approximately 0.36 nm and 0.60 nm are observed in the HRTEM images of $\text{TiO}_2\text{-B@SnS}_2$ heterostructure (Fig. 3b), which are consistent with the (110) and (001) crystal planes of $\text{TiO}_2\text{-B}$ and SnS_2 nanosheets, respectively. Besides, a lattice fringe with a d-spacing of 0.172 nm, 0.357 nm, and 0.352 nm are consistent with the (201) and (110) for $\text{TiO}_2\text{-B}$, (011) for anatase (Fig. S1c), which is in agreement with XRD results. For the $\text{TiO}_2\text{-B@SnS}_2$ hybrids and pure SnS_2 nanoplates, the thickness of nanosheets is estimated to 13 layers and 22 layers, respectively (Fig. 3b and Fig. S1f). Which indicating that the reduction of stack phenomenon due to the introduction of $\text{TiO}_2\text{-B}$ nanobelts. Meanwhile, the coexistence of S, Sn, and Ti elements are homogeneously distributed in the $\text{TiO}_2\text{-B@SnS}_2$ hybrids, which suggest the formation of abundant $\text{TiO}_2\text{-B@SnS}_2$ heterojunctions. The unique heterostructures with a built-in electric field and the few-layered SnS_2 nanosheets can improve the insertion/extraction ability of Li^+ during the charge/discharge process, rendering a better rate capability and suppressing the volume collapse.

XPS analysis was performed to obtain more details about the elemental information and surface electronic states of pure SnS_2 and $\text{TiO}_2\text{-B@SnS}_2$ hybrids. The results suggest that the hybrids contain the main elements of Sn, S, Ti, and (Fig. 4a). The high-resolution Ti 2p spectrum (Fig. 4b) displays two major peaks at 458.9, 464.6 eV and 459.6, 465.3 eV for $\text{TiO}_2\text{-B}$ nanobelts and $\text{TiO}_2\text{-B@SnS}_2$ hybrids, respectively, which corresponding to Ti 2p_{3/2} and Ti 2p_{1/2} (Fig. 4b)^[25, 21]. The separated XPS spectra of Sn 3d (Fig. 4c) at 495.6, 487.2 eV for SnS_2 and 495.4, 487.0 eV for $\text{TiO}_2\text{-B@SnS}_2$ hybrids, which are attributed to Sn 3d_{3/2} and Sn 3d_{5/2}^[26, 17]. Furthermore, the high-resolution S 2p peaks of (Fig. 4d) at 163.4, 162.2 eV for SnS_2 and 163.2, 162.0 eV for $\text{TiO}_2\text{-B@SnS}_2$ hybrids, corresponding to S 2p_{1/2} and S 2p_{3/2}. The above results show that the peaks shift to higher banding energy for Ti 2p, while the peaks shift to lower banding energy for Sn 3d and S 2p after the introduction of $\text{TiO}_2\text{-B}$ nanobelts. This

phenomenon indicated that the electrons transfer from $\text{TiO}_2\text{-B}$ nanobelts to SnS_2 after incorporation, confirming the formation of n-n type heterojunction at the $\text{TiO}_2\text{-B@SnS}_2$ interface^[1, 20]. The specific heterojunction structure will be enhanced the charge transfer and Li^+ diffusion kinetics at the $\text{TiO}_2\text{-B@SnS}_2$ interface, leading to the improvement of electrochemical performance.

In order to reveal the effect of unique heterojunction structure on the electrochemical performance for $\text{TiO}_2\text{-B@SnS}_2$ hybrids. The electrochemical performance of $\text{TiO}_2\text{-B@SnS}_2$ hybrids as the anode materials for LIBs has been evaluated using CV and discharge/charge tests. The CV profiles of SnS_2 and $\text{TiO}_2\text{-B@SnS}_2$ electrode at a scanning rate of 0.1 mV s^{-1} are shown in Fig. 5a and **Fig. S2**, respectively. Two obvious oxidation peaks at around 0.50 and 1.65 V and three reduction peaks at 0.20, 1.25 and 1.71 V are observed in the first cycle of CV profiles for both SnS_2 and $\text{TiO}_2\text{-B@SnS}_2$ electrode (Fig. 5a and **Fig. S2**). Meanwhile, the conversion reaction process of SnS_2 to Sn and Li_2S is corresponded to the reduction peak at 1.25 V, together with the formation of solid electrolyte interphase (SEI), while the broad peak at 0.20 V should be attributed to the multi-step alloying reaction of Sn and Li. Compare to the CV profile of SnS_2 , the reduction and oxidation peaks have no change for $\text{TiO}_2\text{-B@SnS}_2$ electrode, which indicated that the introduction of $\text{TiO}_2\text{-B}$ nanobelts did not effect the electrochemical reaction. In the oxidation scan, a broad peak at 0.50 V is originated from the multi-step dealloying reaction of Li_xSn . While the peak at 1.65 V is indexed to the conversion reaction from Sn to SnS_2 . Furthermore, the discharge/charge behavior of SnS_2 and $\text{TiO}_2\text{-B@SnS}_2$ hybrids anodes in the potential window of 0.01-3.0 V at 0.1 C is shown in Fig. 5b and **Fig. S3a**. The SnS_2 electrode exhibits the initial discharge capacity of 752.8 mAh g^{-1} , while it rapidly decreases to 448.1 mAh g^{-1} after three cycles. In contrast, the $\text{TiO}_2\text{-B@SnS}_2$ displays a higher discharge capacity of $1056.6 \text{ mAh g}^{-1}$ at the first cycle and 622.3 mAh g^{-1} after three cycles. This phenomenon indicates the higher specific capacity because of improve reversibility of alloy reaction after the construction of heterojunction structure. Meanwhile, the rate performance of the as-prepared SnS_2 and $\text{TiO}_2\text{-B@SnS}_2$ samples at various current densities from 0.1 to 15 C is displayed in Fig. 5c, d and **Fig. S3b**. As expected, the $\text{TiO}_2\text{-B@SnS}_2$ shows the high discharge capacity of 1056.6, 488.3, 365.7, 270.2, 202.6, 146.9, and 110.4 mAh g^{-1} at 0.1, 0.2, 0.5, 1, 2, 5, and 10 C, respectively. Even at a high rate of 15 C, a discharge capacity 81.2 mAh g^{-1} can be obtained. However, the discharge capacity decreased quickly for the SnS_2 electrode, particularly under high rate of 10 and 15 C, where it only exhibits 17.0 and 9.8 mAh g^{-1} , respectively. Furthermore, the cycling performance at high rate of 5 C is also studied (Fig. 5e). The $\text{TiO}_2\text{-B@SnS}_2$ electrode exhibits a higher reversible capacity (127.7 mAh g^{-1}) after 200 cycles. In contrast, the discharge capacity approaches to zero after 100 cycles for SnS_2 electrode. The high rate capability and excellent cycling stability of $\text{TiO}_2\text{-B@SnS}_2$ composite is attributed to the unique heterojunction structure between the $\text{SnS}_2/\text{TiO}_2\text{-B}$ interface, which could effectively improve Li^+ kinetics and suppress the volume change during the discharge/charge process.

Additionally, the effect of multistep lithiation-delithiation on the ion diffusion and conductivity properties of electrode was investigated. Figure 6a, b and **Eq. S1** show the Galvanostatic Intermittent Titration

Technique (GITT) curves for the fifth cycle of $\text{TiO}_2\text{-B@SnS}_2$ and SnS_2 electrode materials. The increase in D_{Li^+} presented by the $\text{TiO}_2\text{-B@SnS}_2$ electrode is higher than that of SnS_2 , which is a result of conductivity enhancement after the introduction of $\text{TiO}_2\text{-B}$ nanobelts.

To obtain the fundamental insights of the excellent rate performance and cycling stability, the density functional theory (DFT) calculations were performed to further explore the effect of the specific heterojunction structure between the $\text{SnS}_2/\text{TiO}_2\text{-B}$ interface (Fig. 7a-c). The $\text{TiO}_2\text{-B}$ possesses a direct band gap of ~ 1.68 eV, and 1.60 eV for SnS_2 semiconductor. As expected, the $\text{TiO}_2\text{-B@SnS}_2$ sample exhibits a narrow band gap ~ 0.58 eV, indicating the improvement of electronic conductivity because of the unique heterojunction structure between the $\text{SnS}_2/\text{TiO}_2\text{-B}$ interface, which is desirable for high-rate discharging/charging.

3. Conclusions

In summary, nanosheets-constructed porous $\text{TiO}_2\text{-B@SnS}_2$ hybrids has been fabricated by a facile hydrothermal method accompanying the formation heterojunction structure between $\text{SnS}_2/\text{TiO}_2\text{-B}$ interface. The hybrids exhibits higher reversible capacity of 146.9, 110.4, and 81.2 mAh g^{-1} at 5, 10, and 15 C, respectively. Moreover, the $\text{TiO}_2\text{-B@SnS}_2$ electrode exhibits a higher reversible capacity (127.7 mAh g^{-1}) after 200 cycles at 5 C. The excellent rate capability and cycling stability of the composite is attributed to the unique heterojunction structure between SnS_2 and $\text{TiO}_2\text{-B}$ interface, which provides a fast transmission channel for Li^+ and improves structural stability of electrode material during the lithium storage process. Additionally, few-layers SnS_2 nanosheets were obtained due to the introduction of $\text{TiO}_2\text{-B}$ nanobelts, which shorted the transmission distance of Li^+ .

Declarations

Conflicts of interest

The author declare no competing financial interests.

Funding

This work was supported by the National Natural Science Foundation of China (No. 51961034, No. 51741107), Key Research and Development Program of Ningxia (Talent Projects: 2018BEB04037) and Hunan Provincial Department of Education Project (20C0153).

References

1. Wu L, Zheng J, Wang L, Xiong X, Shao Y, Wang G, Wang JH, Zhong S, Wu M (2019) PPy-encapsulated SnS₂ Nanosheets Stabilized by Defects on a TiO₂ Support as a Durable Anode Material for Lithium-Ion Batteries. *Angew Chem Int Ed Engl* 58 (3):811-815. doi:10.1002/anie.201811784
2. Huang S, Wang M, Jia P, Wang B, Zhang J, Zhao Y (2019) N-graphene motivated SnO₂@SnS₂ heterostructure quantum dots for high performance lithium/sodium storage. *Energy Storage Materials* 20:225-233. doi:10.1016/j.ensm.2018.11.024
3. An C-s, Zhang B, Tang L-b, Xiao B, He Z-j, Zheng J-c (2019) Binder-free carbon-coated TiO₂@graphene electrode by using copper foam as current collector as a high-performance anode for lithium ion batteries. *Ceramics International* 45 (10):13144-13149. doi:10.1016/j.ceramint.2019.03.249
4. Sultana I, Rahman MM, Mateti S, Ahmadabadi VG, Glushenkov AM, Chen Y (2017) K-ion and Na-ion storage performances of Co₃O₄-Fe₂O₃ nanoparticle-decorated super P carbon black prepared by a ball milling process. *Nanoscale* 9 (10):3646-3654. doi:10.1039/C6NR09613A
5. Xia J, Liu L, Jamil S, Xie J, Yan H, Yuan Y, Zhang Y, Nie S, Pan J, Wang X, Cao G (2019) Free-standing SnS/C nanofiber anodes for ultralong cycle-life lithium-ion batteries and sodium-ion batteries. *Energy Storage Materials* 17:1-11. doi:https://doi.org/10.1016/j.ensm.2018.08.005
6. Deng Z, Jiang H, Hu Y, Liu Y, Zhang L, Liu H, Li C (2017) 3D Ordered Macroporous MoS₂@C Nanostructure for Flexible Li-Ion Batteries. *Advanced Materials*:1603020. doi:10.1002/adma.201603020
7. Wang L, Guo H, Wang W, Teng K, Xu Z, Chen C, Li C, Yang C, Hu C (2016) Preparation of sandwich-like phosphorus/reduced graphene oxide composites as anode materials for lithium-ion batteries. *Electrochimica Acta* 211:499-506. doi:10.1016/j.electacta.2016.06.052
8. Yuan Y, Xiao W, Wang Z, Fray DJ, Jin X (2018) Efficient Nanostructuring of Silicon by Electrochemical Alloying/Dealloying in Molten Salts for Improved Lithium Storage. *Angew Chem Int Ed Engl*. doi:10.1002/anie.201809646
9. Liu J, Gu M, Ouyang L, Wang H, Yang L, Zhu M (2016) Sandwich-like SnS/Polypyrrole Ultrathin Nanosheets as High-Performance Anode Materials for Li-Ion Batteries. *ACS Appl Mater Interfaces* 8 (13):8502-8510. doi:10.1021/acsami.6b00627
10. Li X, Guo G, Qin N, Deng Z, Lu Z, Shen D, Zhao X, Li Y, Su BL, Wang HE (2018) SnS₂/TiO₂ nanohybrids chemically bonded on nitrogen-doped graphene for lithium-sulfur batteries: synergy of vacancy defects and heterostructures. *Nanoscale* 10 (33):15505-15512. doi:10.1039/c8nr04661a
11. Wang H-E, Zhao X, Li X, Wang Z, Liu C, Lu Z, Zhang W, Cao G (2017) rGO/SnS₂/TiO₂ heterostructured composite with dual-confinement for enhanced lithium-ion storage. *Journal of Materials Chemistry A* 5 (47):25056-25063. doi:10.1039/c7ta08616d
12. An C, Yuan Y, Zhang B, Tang L, Xiao B, He Z, Zheng J, Lu J (2019) Graphene Wrapped FeSe₂ Nano-Microspheres with High Pseudocapacitive Contribution for Enhanced Na-Ion Storage. *Advanced*

- Energy Materials 9 (18). doi:10.1002/aenm.201900356
13. Sun H, Ahmad M, Luo J, Shi Y, Shen W, Zhu J (2014) SnS₂ nanoflakes decorated multiwalled carbon nanotubes as high performance anode materials for lithium-ion batteries. *Materials Research Bulletin* 49:319-324. doi:10.1016/j.materresbull.2013.09.005
 14. Li J, Wang M, Huang J (2021) Bio-inspired hierarchical nanofibrous SnS/C composite with enhanced anodic performances in lithium-ion batteries. *Journal of Alloys and Compounds* 860:157897. doi:https://doi.org/10.1016/j.jallcom.2020.157897
 15. Li J, Zhang S, Zhang S, An C, Cao L (2021) Templated constructing honeycomb-like V₅S₈@C anode with multi-scale interfacial coactions and high pseudocapacitive contribution for enhanced potassium storage capability. *Journal of Alloys and Compounds* 851. doi:10.1016/j.jallcom.2020.156920
 16. Wang J, Huang J, Huang S, Notohara H, Urita K, Moriguchi I, Wei M (2020) Rational Design of Hierarchical SnS₂ Microspheres with S Vacancy for Enhanced Sodium Storage Performance. *ACS Sustainable Chemistry & Engineering* 8 (25):9519-9525. doi:10.1021/acssuschemeng.0c02535
 17. Luo B, Fang Y, Wang B, Zhou J, Song H, Zhi L (2012) Two dimensional graphene-SnS₂ hybrids with superior rate capability for lithium ion storage. *Energy Environ Sci* 5 (1):5226-5230. doi:10.1039/c1ee02800f
 18. Feng X, Li J, Ma Y, Yang C, Zhang S, Li J, An C (2021) Construction of Interlayer-Expanded MoSe₂/Nitrogen-Doped Graphene Heterojunctions for Ultra-Long-Cycling Rechargeable Aluminum Storage. *ACS Applied Energy Materials* 4 (2):1575-1582. doi:10.1021/acsaem.0c02797
 19. Li Y, Qian J, Zhang M, Wang S, Wang Z, Li M, Bai Y, An Q, Xu H, Wu F, Mai L, Wu C (2020) Co-Construction of Sulfur Vacancies and Heterojunctions in Tungsten Disulfide to Induce Fast Electronic/Ionic Diffusion Kinetics for Sodium-Ion Batteries. *Advanced Materials*:2005802. doi:10.1002/adma.202005802
 20. Zheng Y, Zhou T, Zhang C, Mao J, Liu H, Guo Z (2016) Boosted Charge Transfer in SnS/SnO₂ Heterostructures: Toward High Rate Capability for Sodium-Ion Batteries. *Angewandte Chemie International Edition* 55 (10):3408-3413. doi:https://doi.org/10.1002/anie.201510978
 21. Liu S, Jia H, Han L, Wang J, Gao P, Xu D, Yang J, Che S (2012) Nanosheet-constructed porous TiO₂-B for advanced lithium ion batteries. *Adv Mater* 24 (24):3201-3204. doi:10.1002/adma.201201036
 22. Armstrong AR, Armstrong G, Canales J, Bruce PG (2005) TiO₂-B nanowires as negative electrodes for rechargeable lithium batteries. *Journal of Power Sources* 146 (1):501-506. doi:https://doi.org/10.1016/j.jpowsour.2005.03.057
 23. Chao D, Liang P, Chen Z, Bai L, Shen H, Liu X, Xia X, Zhao Y, Savilov SV, Lin J, Shen ZX (2016) Pseudocapacitive Na-Ion Storage Boosts High Rate and Areal Capacity of Self-Branched 2D Layered Metal Chalcogenide Nanoarrays. *ACS Nano* 10 (11):10211-10219. doi:10.1021/acsnano.6b05566
 24. Zhang Y, Zhu P, Huang L, Xie J, Zhang S, Cao G, Zhao X (2015) Few-Layered SnS₂ on Few-Layered Reduced Graphene Oxide as Na-Ion Battery Anode with Ultralong Cycle Life and Superior Rate

25. Liu H, Zhang S, Chen Y, Zhang J, Guo P, Liu M, Lu X, Zhang J, Wang Z (2018) Rational design of TiO_2 @nitrogen-doped carbon coaxial nanotubes as anode for advanced lithium ion batteries. Applied Surface Science 458:1018-1025. doi:10.1016/j.apsusc.2018.07.156
26. Zhang Z, Shao C, Li X, Sun Y, Zhang M, Mu J, Zhang P, Guo Z, Liu Y (2013) Hierarchical assembly of ultrathin hexagonal SnS_2 nanosheets onto electrospun TiO_2 nanofibers: enhanced photocatalytic activity based on photoinduced interfacial charge transfer. Nanoscale 5 (2):606-618. doi:10.1039/c2nr32301j

Figures

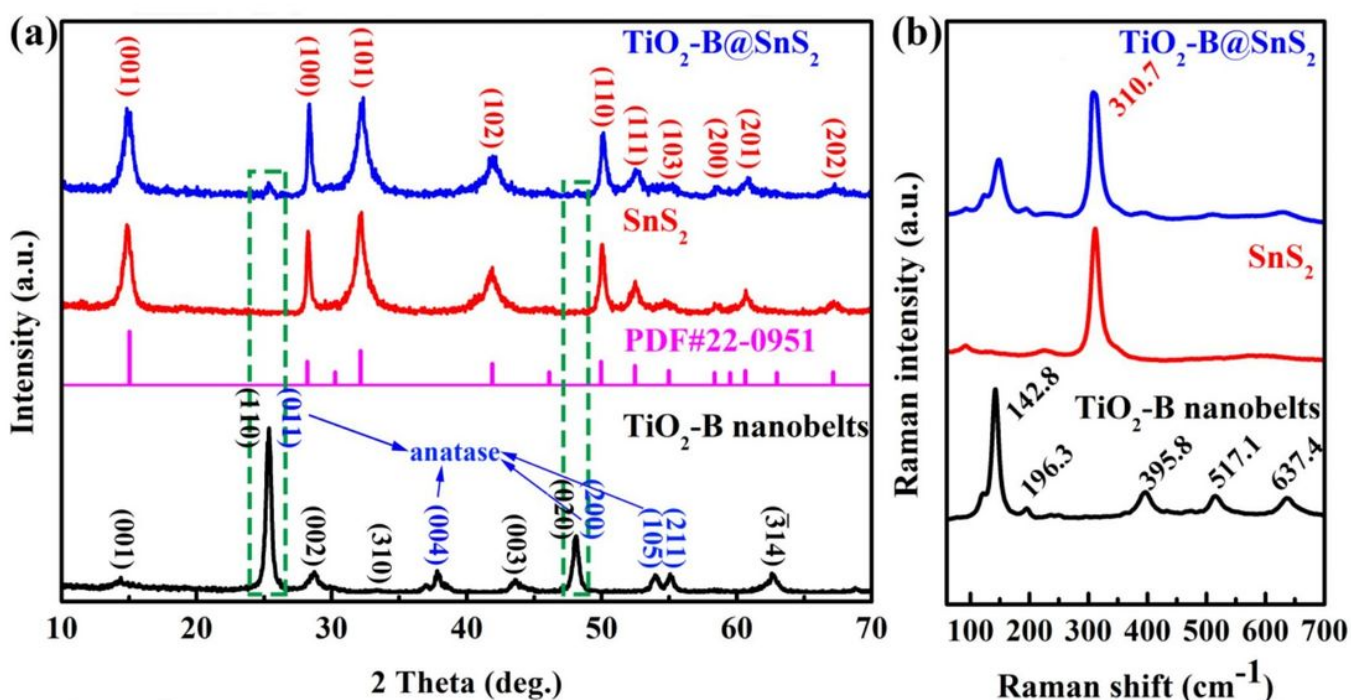


Fig. 1

Figure 1

XRD patterns (a) and Raman spectrum (b) of the $\text{TiO}_2\text{-B nanobelts}$, SnS_2 and $\text{TiO}_2\text{-B@SnS}_2$.

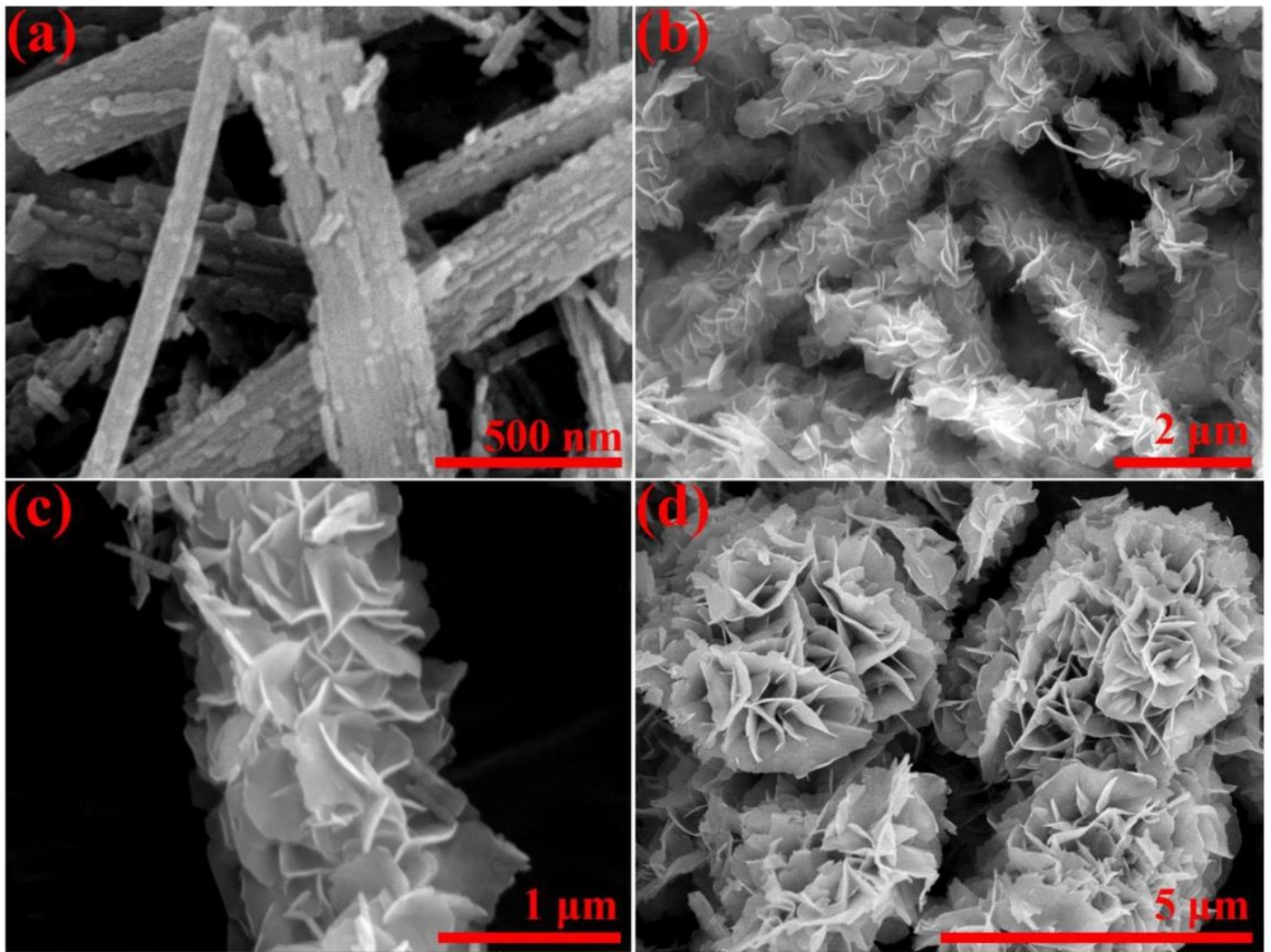


Fig. 2

Figure 2

SEM images of the TiO₂-B nanobelts (a), TiO₂-B@SnS₂ (b, c) and SnS₂ (c).

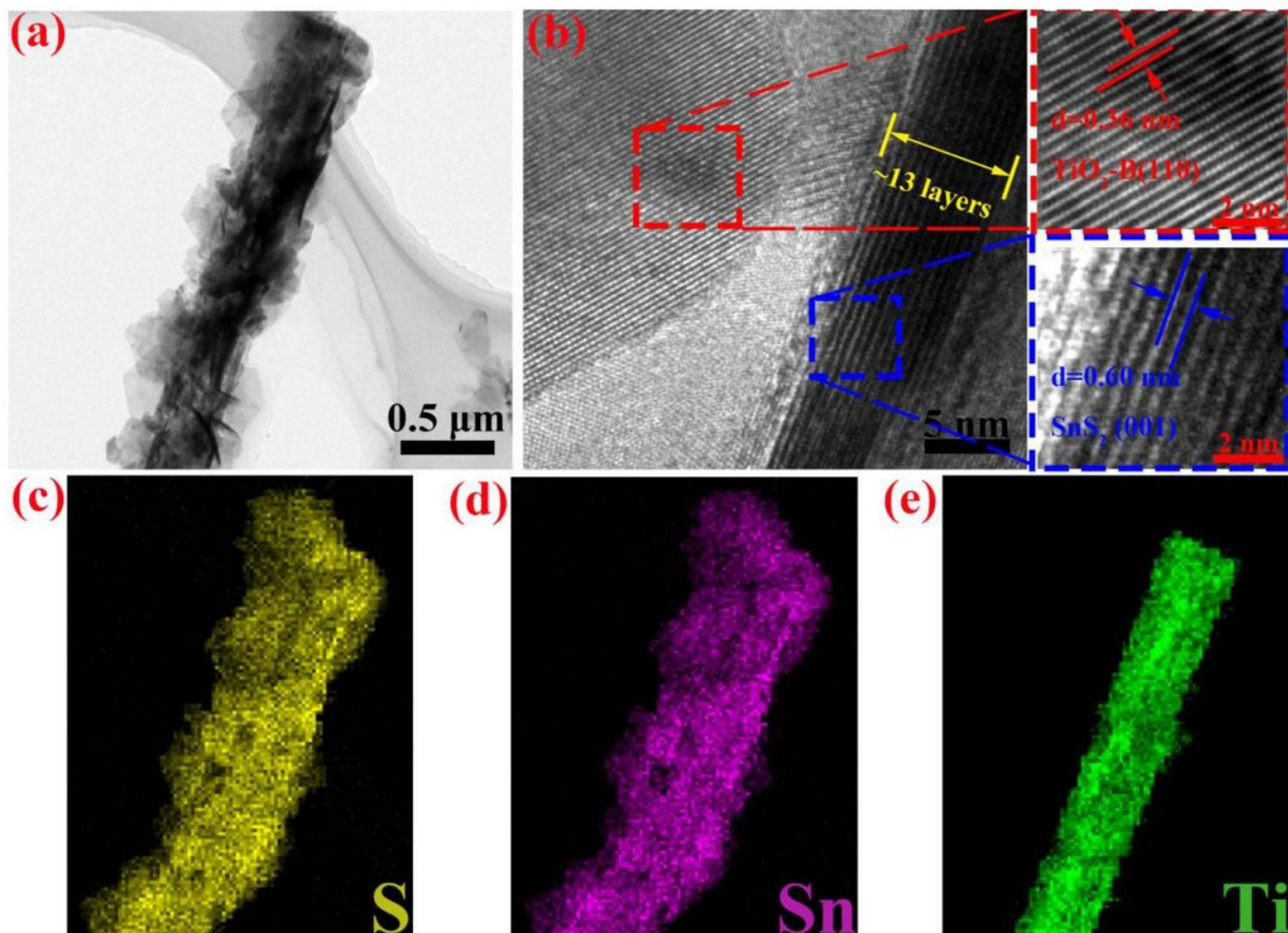


Fig. 3

Figure 3

High-magnification TEM image (a), HRTEM image (b), elemental mapping image (c, d, and e) of the $\text{TiO}_2\text{-B@SnS}_2$, respectively.

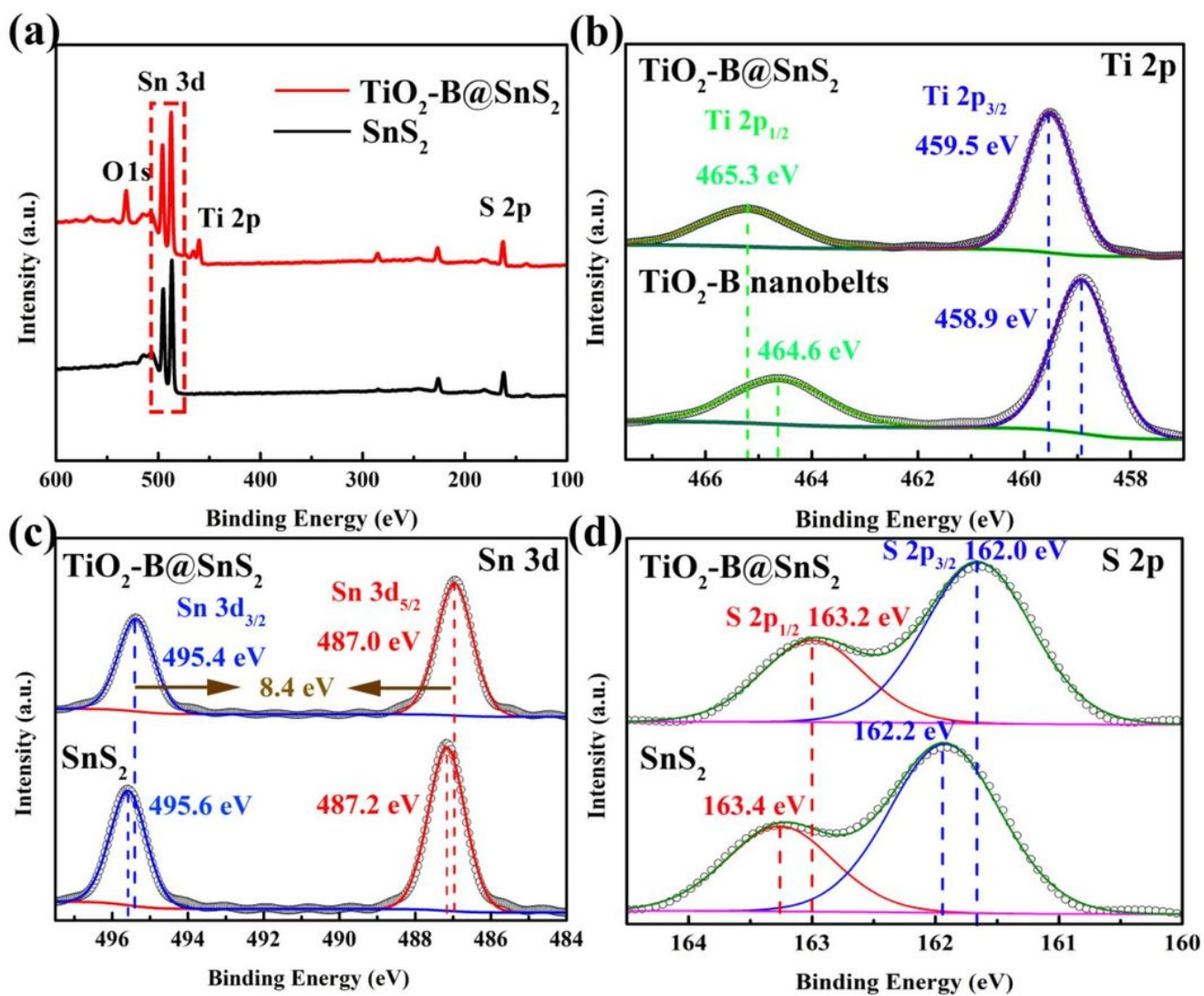


Fig. 4

Figure 4

XPS spectra of SnS_2 and $\text{TiO}_2\text{-B@SnS}_2$. (a) survey spectrum, and (b) Ti 2p, (c) Sn 3d, (d) O 1s and S 2p, respectively.

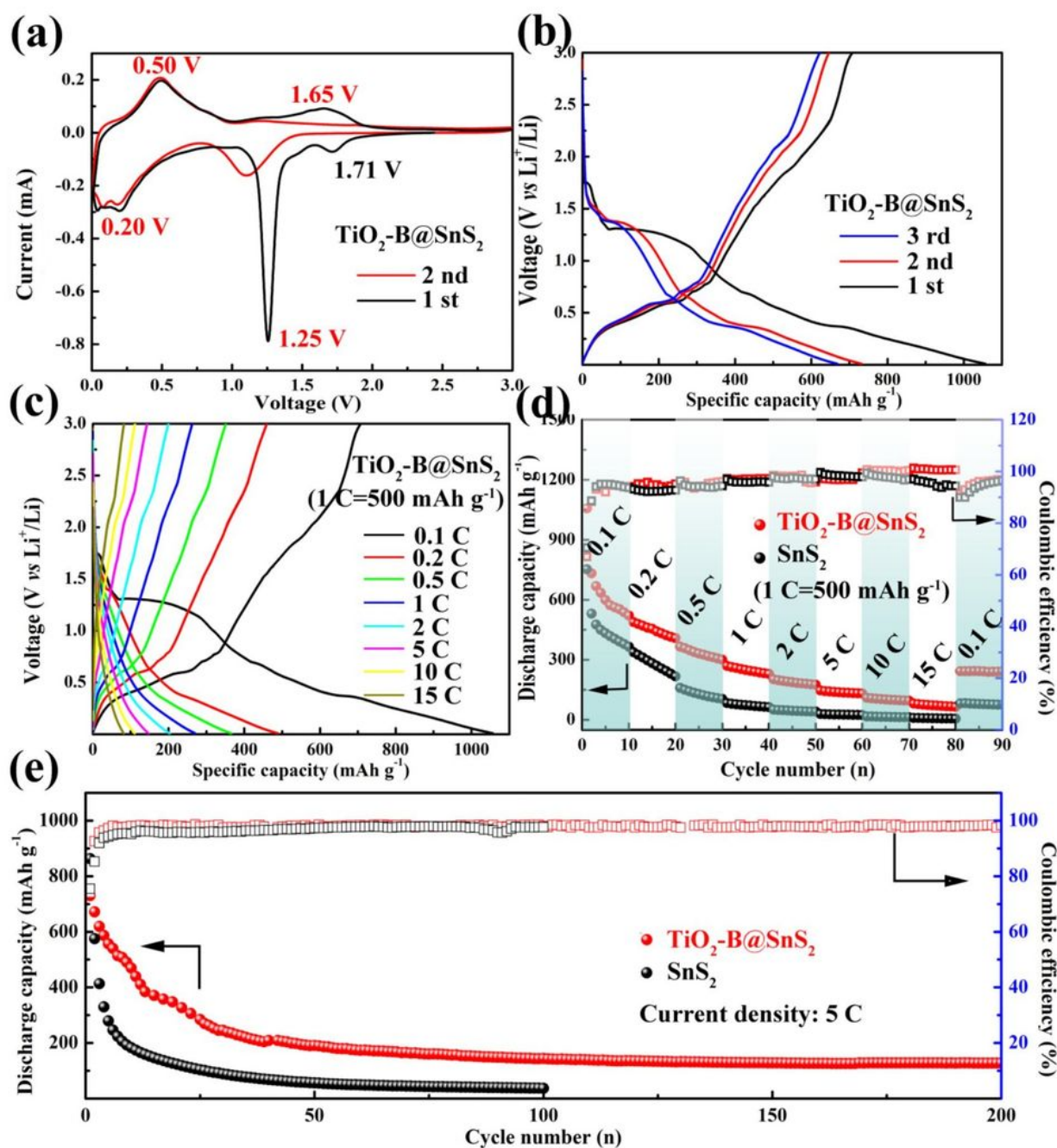


Fig. 5

Figure 5

Electrochemical performance of SnS₂ and TiO₂-B@SnS₂ electrode. (a) Cyclic voltammetry (CV) curves at a scanning of 0.1 mV s⁻¹ in the voltage range of 0.01-3.0 V versus Li⁺/Li, discharge/charge profiles during three cycles at a rate of 0.1 C (b), and the first discharge/charge cycle at different discharge current densities (c) of TiO₂-B@SnS₂. Rate capability at various current densities from 0.1 to 15 C (d), long-term cycling performance at a cyclic rate of 5 C (e) of SnS₂ and TiO₂-B@SnS₂.

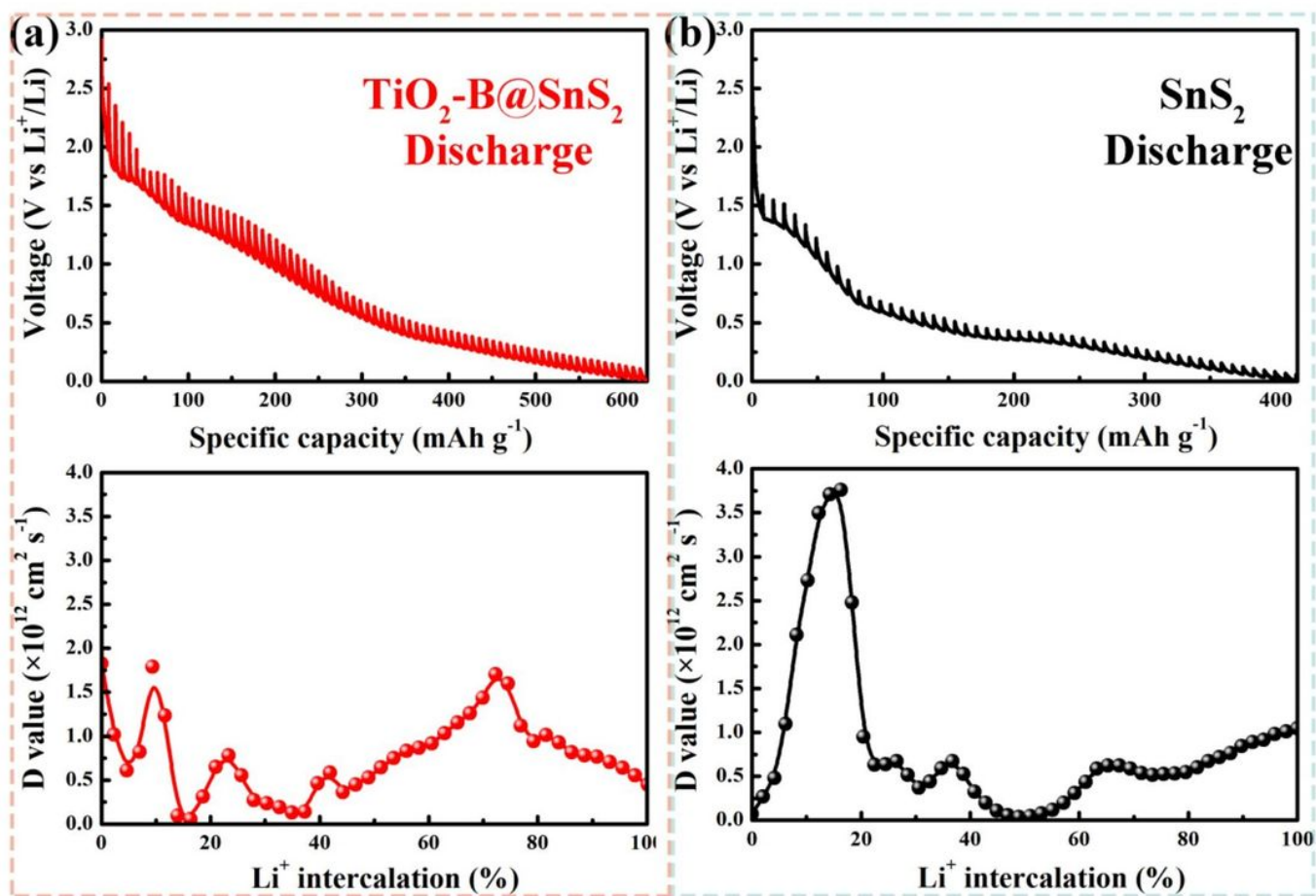


Fig. 6

Figure 6

Discharge/Charge curves of $\text{TiO}_2\text{-B@SnS}_2$ (a) and SnS_2 (b) in GITT measurement and corresponding diffusivity coefficient (D) of Li^+ in the discharge/charge process.

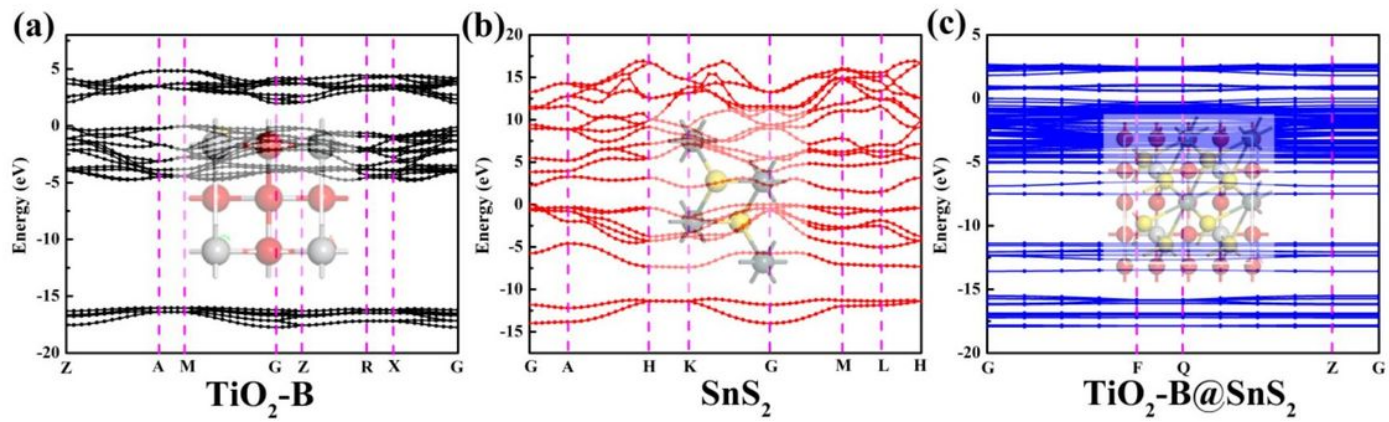
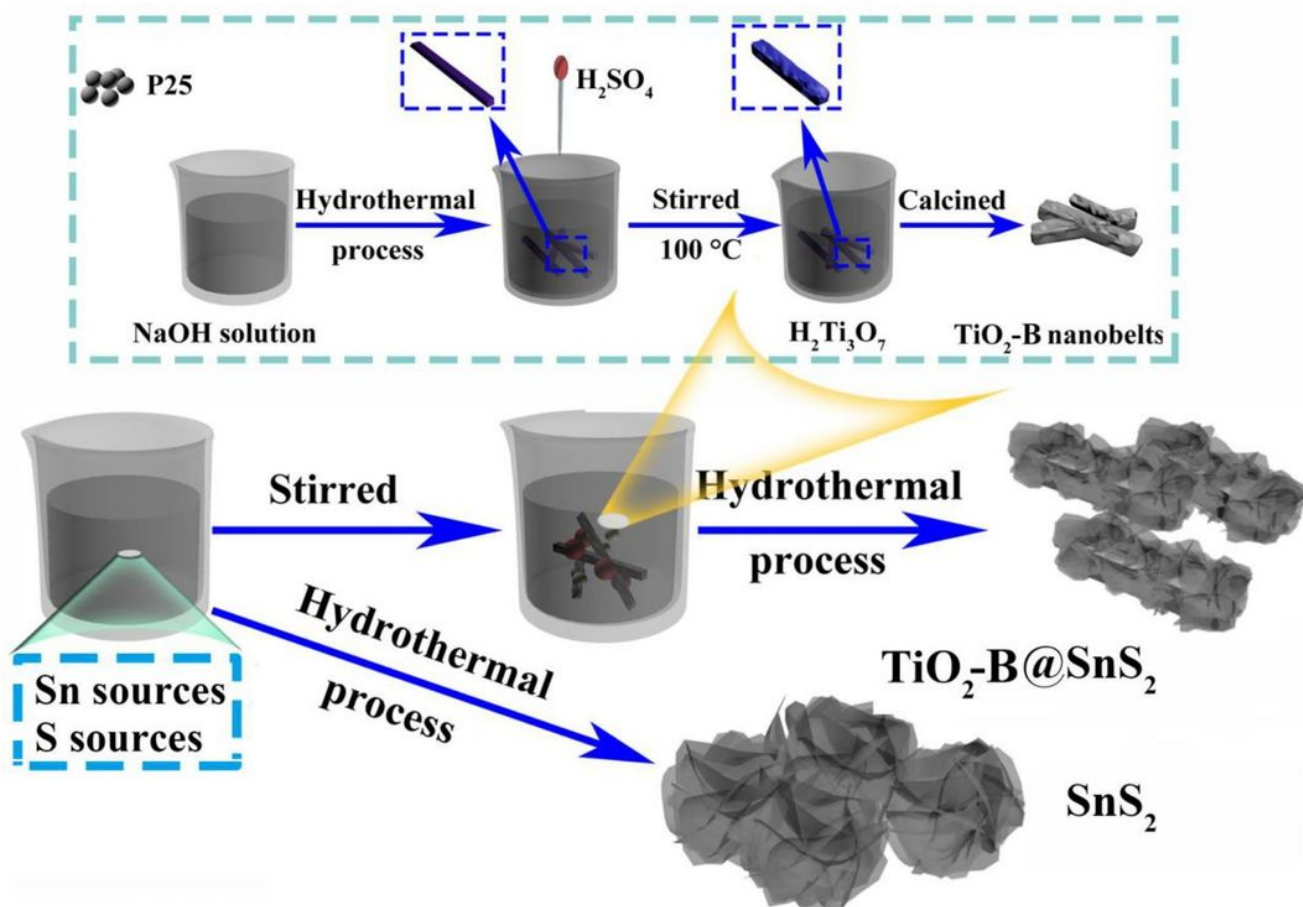


Fig. 7

Figure 7

Band structure for $\text{TiO}_2\text{-B}$ (a), SnS_2 (b) and $\text{TiO}_2\text{-B@SnS}_2$ (c).



Scheme 1

Figure 8

Illustration of the fabrication of TiO₂-B nanobelts and TiO₂-B@SnS₂ hybrids.

Supplementary Files

This is a list of supplementary files associated with this preprint. Click to download.

- [supportinformation.docx](#)